GDCh Research Article Angewandte International Edition Chemie www.angewandte.org

Check for updates

How to cite: *Angew. Chem. Int. Ed.* **2025**, *64*, e20907
doi.org/10.1002/anie.202520907

CO_2-to-CO Catalysis Hot Paper

Substituent-Generated Electric Fields and Ligand Non-Innocence Drive the Record-High Efficiency of Iron Tetraphenylporphyrin Catalysts for CO_2-to-CO Conversion

*Purva Dua and Gopalan Rajaraman**

Abstract: Electrochemical CO_2-to-CO conversion is a critical step in sustainable catalysis, with iron-tetraphenylporphyrin (Fe–TPP) derivatives recognised as benchmark catalysts, reaching turnover frequencies (TOFs) up to 10^6 s^{-1} with trimethylammonium (TMA) substitution. However, substituent effects remain unpredictable: sulfonyl groups render the catalyst inactive, while others enhance activity, yielding over 50 analogues without coherent design principle. Using density functional theory (DFT) and response theory (including electric field effects), we identify factors governing this variability. Electronic structure analysis reveals the redox non-innocent behaviour of TPP ligand, forming $[Fe(II)TPP^{\bullet\bullet}]^{2-}$ species, stabilised by antiferromagnetic coupling ($J = -656$ cm^{-1}). The ligand's ability to transiently hold and transfer electrons during the catalytic cycle enhances catalytic performance. Energetic-span model analysis for Fe–TPP (**1**), Fe–p-TMA (**2**), and Fe–o-TMA (**3**) yields barriers of 195.5, 184.4, and 162.2 kJ mol^{-1}, respectively, matching experiments **3** > **2** > **1**. Crucially, local electric fields (LEFs), arising from charged substituents dominate reactivity, surpassing traditional steric or inductive considerations. Applying an oriented electric field of + 0.21 V $Å^{-1}$ to **1** reproduces the performance of **3**, confirming LEF as a unifying descriptor. Guided by this, we in silico design next-generation catalysts, setting a new paradigm in CO_2 reduction catalysis.

Introduction

Converting CO_2 into value-added products is crucial for climate change mitigation and greenhouse gas reduction.[1–4] In 2023, global temperatures saw a record rise of 0.28 °C, highlighting the urgency for innovative solutions.[5] Transforming CO_2 into useful chemicals not only tackles environmental issues but also provides a sustainable pathway for generating essential resources.[6–11] Among various CO_2 conversion strategies—chemical, photocatalytic, and electrocatalytic methods—electrochemical CO_2 reduction (CO_2RR) has gained significant attention for its efficiency in producing valuable intermediates like carbon monoxide (CO) and formic acid.[12,13] Between these two intermediates, CO, a key component of synthetic gas, is a versatile intermediate in Fischer–Tropsch chemistry for producing valuable organic compounds.[14,15] This process can proceed via two main strategies: direct photochemical systems that harness sunlight to convert CO_2 or indirect systems that first generate solar electricity to drive electrochemical reduction. However, the high energy requirement for the formation of the CO_2 anion radical ($CO_2^{\bullet-}$) at −1.97 V versus SHE[16] necessitates catalytic systems to lower the activation barrier and improve reaction efficiency. Transition-metal complexes, particularly iron porphyrins, have emerged as promising catalysts for CO_2-to-CO conversion (Scheme 1).[17] Despite their potential, these catalysts often suffer from limited efficiency and rapid degradation, hindering their practical applicability.[18,19]

Among the list of catalysts reported (Scheme 1 and Table S1) for the CO_2-to-CO conversion, iron porphyrin-based complexes gain attention due to their versatile nature and high selectivity. Among other factors, substituents at the meso-position of the porphyrin were found to alter the catalytic abilities significantly. For example, Fe–porphyrin with four sulfonate groups (standard reduction potential of $Fe^{I/0}$ couple, E^0_{cat} =−1.428 V) exhibits significantly lower reactivity than its unsubstituted counterpart, while trimethylamine substitution ($E^0_{cat} = -0.944$ V) at the ortho position of the aryl group enhances catalytic performance dramatically, achieving a turnover frequency of 10^6 s^{-1}—the highest reported among Fe-based catalysts.[20] While substituents were expected to play a role both in terms of steric and electronics in modulating the reactivity, if we gloss over the range of metal catalysts and other complexes reported in the literature (see Table S1). It is evident that substituents possessing cationic charges in the proximity of the metal centre are found to enhance the reactivity. This suggests a possible role of electrostatic interactions and electric fields[21] that are generated due to these charged entities influencing the overall reaction. The electric field generated at the vicinity of the active site, termed as local electric fields (LEFs) is an established concept in enzymatic chemistry wherein many naturally occurring enzymes[22–24] were shown

[*] P. Dua, G. Rajaraman
Department of Chemistry, Indian Institute of Technology Bombay, Powai, Mumbai 400076, India
E-mail: rajaraman@chem.iitb.ac.in

Additional supporting information can be found online in the Supporting Information section

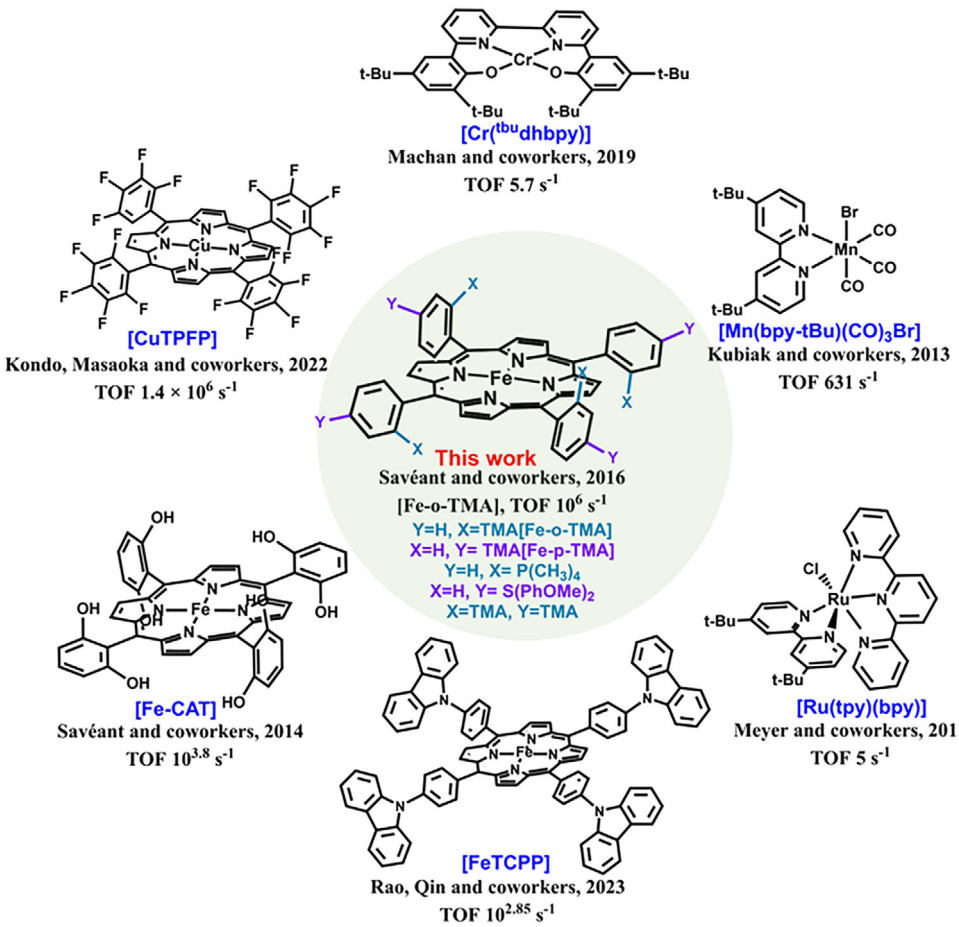

Scheme 1. Various molecular catalysts employed in the electrochemical CO_2-to-CO conversion reaction reported in the literature.

to generate LEFs due to the charged residues that in turn enhance their efficiency. External electric fields can also be applied, though aligning them along specific bonds is difficult in standard electrochemical setups. This has been achieved using STM tips, where oriented external fields (OEEFs)[25,26] have been shown to control regioselectivity in Diels–Alder reactions and enhance catalytic performance. [27,28] This is a rapidly developing area where OEEFs are employed to modulate the chemical reactions and improve catalytic performance.

Building on these findings, here we have explored using a combination of DFT and response theory, such as OEEFs, to answer the following open questions in the area of CO_2-to-CO conversion: (i) how vital are the ligand architecture and its non-innocent character in dictating the efficiency of CO_2-to-CO reduction? (ii) how do key mechanistic barriers influence efficiency? and (iii) what is the interplay between chemically induced local electric fields and catalytic performance, and how can OEEFs be utilised to optimise reactivity? To answer these three key questions, we have studied the CO_2-to-CO conversion for Fe–porphyrin systems—FeTPP (**1**), Fe–p-TMA (**2**), and Fe–o-TMA (**3**) with phenol as co-additive and dimethyl-formamide as solvent (see computational details for more information and see Tables S2 and S3).

Results and Discussions

Formation of Fe(0) Catalysts 1–3

For the electrocatalytic process, the initial precursor consists of ***1–r***, ***2–r***, and ***3–r***, where ***r*** represents (L)Fe(III)–Cl (L = TPP (**1**), *p*-TMA (**2**), *o*-TMA (**3**)). This precursor undergoes electrochemical reduction to form a Fe(II)Cl complex, initiating the catalytic cycle. For this species, calculations predict high-spin S = 5/2 as the ground state for all three species with the S = 3/2 (55.3, 7.9, and 4.8 kJ mol^{-1} for ***1–r*** to ***3–r***, respectively) lying very close in energy and a S = $\frac{1}{2}$ much higher (64.3, 61.1, and 48.7 kJ mol^{-1} for ***1–r*** to ***3–r***, respectively), as shown in Figures S1–S3. The predicted high-spin ground state is consistent with the experimental reports.[29] The geometry of the ^{6}***r*** is found to be distorted square pyramidal with Fe(III) ion above the basal plane by ~0.5 Å. In the next step, this species undergoes a favourable one-electron reduction to form Fe(II)–Cl (***int1***; note that other alternative pathways are higher in energy, Scheme S1). The reduction is exothermic by −42.6, −77.7, and −92.9 kJ mol^{-1} for ***1–int1*** to ***3–int1***, respectively. Among these, the Fe(II) ion in ***1–int1*** lies higher above the {N4} basal plane compared to ***3–int1***, leading to stronger Fe–N bonds in

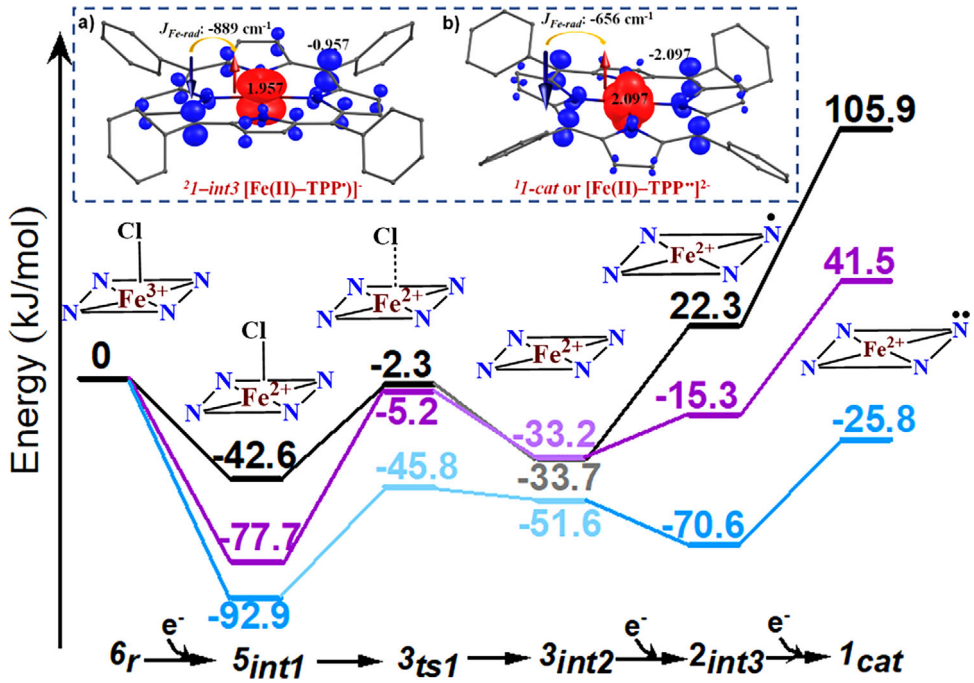

Figure 1. Potential energy surface (PES; ΔG) for the formation of active catalyst [Fe(II)-TPP$^{\bullet\bullet}$]$^{2-}$ for the ground spin states of complex **1**(black), **2**(purple), **3**(blue). The colour variation shows the spin transition through MECP. The inset shows the DFT-computed ground state spin density plot of a) ***^{2}1-int3***, and b) ***^{1}1-cat***, along with the *J* values.

the latter and facilitating a more favourable reduction (see Figures S4–S6).

Subsequently, chloride dissociation occurs via transition state ***ts1***, with energy barriers of 40.3 kJ mol^{-1} (***1–ts1***), 72.5 kJ mol^{-1} (***2–ts1***), and 47.1 kJ mol^{-1} (***3–ts1***). The calculated energy barriers are consistent with earlier reports showing halide dissociation can be endergonic in nonpolar solvents [30] and also consistent with earlier experimental reports that suggest that this step is key in the production of active Fe(II)-TPP species, and the associated energetic cost is more than compensated by the applied electrode potential (see Figure S7).[31] The intermediate ***int2***, formed on the triplet surface, exhibits the lowest barrier for ***3–int2*** at −51.6 kJ mol^{-1}. In the next step, ***int2*** undergoes two successive one-electron reductions to form ***int3*** and the Fe(0) catalyst (***cat***). The first (second) reduction yields formal Fe(I) (Fe(0)) with S = 1/2 (S = 0) as the ground state. Spin densities at Fe and TPP are 1.957 (2.097) and −0.957 (−2.097) for ***1–int3*** (***1–cat***), indicating ligand-based reductions (see Figure 1). Across the reductions, the Fe centre remains in an intermediate-spin Fe(II) (S_{Fe} = 1) state, in ***1–int3*** a very strong antiferromagnetic coupling between the radical generated on the porphyrin ring and Fe centre was detected ($J_{Fe\text{-}rad}$ = −889 cm^{-1}) while for ***1–cat*** a relatively weaker $J_{Fe\text{-}rad}$ (−656 cm^{-1}) was witnessed due to longer ~Fe–N bond length. Such a strong exchange interaction is due to a favourable overlap between the Fe(d_{xz}/d_{yz}) orbitals and the π^* orbital of the TPP ligand. Eigenvalue plot also shows triplet $^3A_{2g}$ [$(d_{xy})^2(d_{z^2})^1(d_{xy},d_{yz})^3$)] electronic configuration, favouring [Fe(II)TPP$^{\bullet-}$]$^-$ ([Fe(II)TPP$^{\bullet\bullet}$]$^{2-}$) rather than [Fe(I)TPP]$^-$ ([Fe(I)TPP]$^{2-}$) (see Figure S8) and this is also consistent with the earlier theoretical and spectral data such as Mössbauer, X-ray absorption, and resonance Raman spectroscopy.[32,33] More importantly, the redox non-innocence is key to the CO_2 activation (see Figure 1, inset). For the other two catalysts, a similar trend is observed, with only minor variations in spin densities, indicating that the substituents have had little impact on the underlying electronic structure (see Figure S8, Tables S5–S7).

Mechanism of CO_2-to-CO conversion

In the next step, the [Fe(II)TPP$^{\bullet\bullet}$]$^{2-}$ (***cat***) is expected to bind to CO_2, and this is facilitated by the formation of a reactant complex (***rc***). The formation of ***rc*** is endothermic by 47.0, 49.3, and 20.3 kJ mol^{-1} for ***1–rc*** to ***3–rc***, respectively. Among the three, ***3–rc*** formation is the least endothermic, thanks to stronger noncovalent interactions between the oxygen atom of CO_2 and *o*-TMA hydrogens (O•••H = 2.598 Å, 2.554 Å; see Figures S8–S12). The strong C–H•••O(CO) interactions were found to activate CO_2, as evidenced by the elongation of the C—O bond and bending of the O—C—O angle by approximately 4–6°. This activation is accompanied by the stabilisation of the triplet as the ground state, as these interactions alter the spin density on the TPP radical, inducing an open-shell singlet biradical character coupled with a triplet state of Fe. In the next step, CO_2 binds to the Fe centre (***int4***) in catalysts **1** and **3**, albeit endergonically, while in catalyst **2**, this binding occurs only in the presence of phenol (***int4'***; +16.5 kJ mol^{-1}), indicating a subtle dependence on its presence. Analogous species in **1** and **3** show favourable

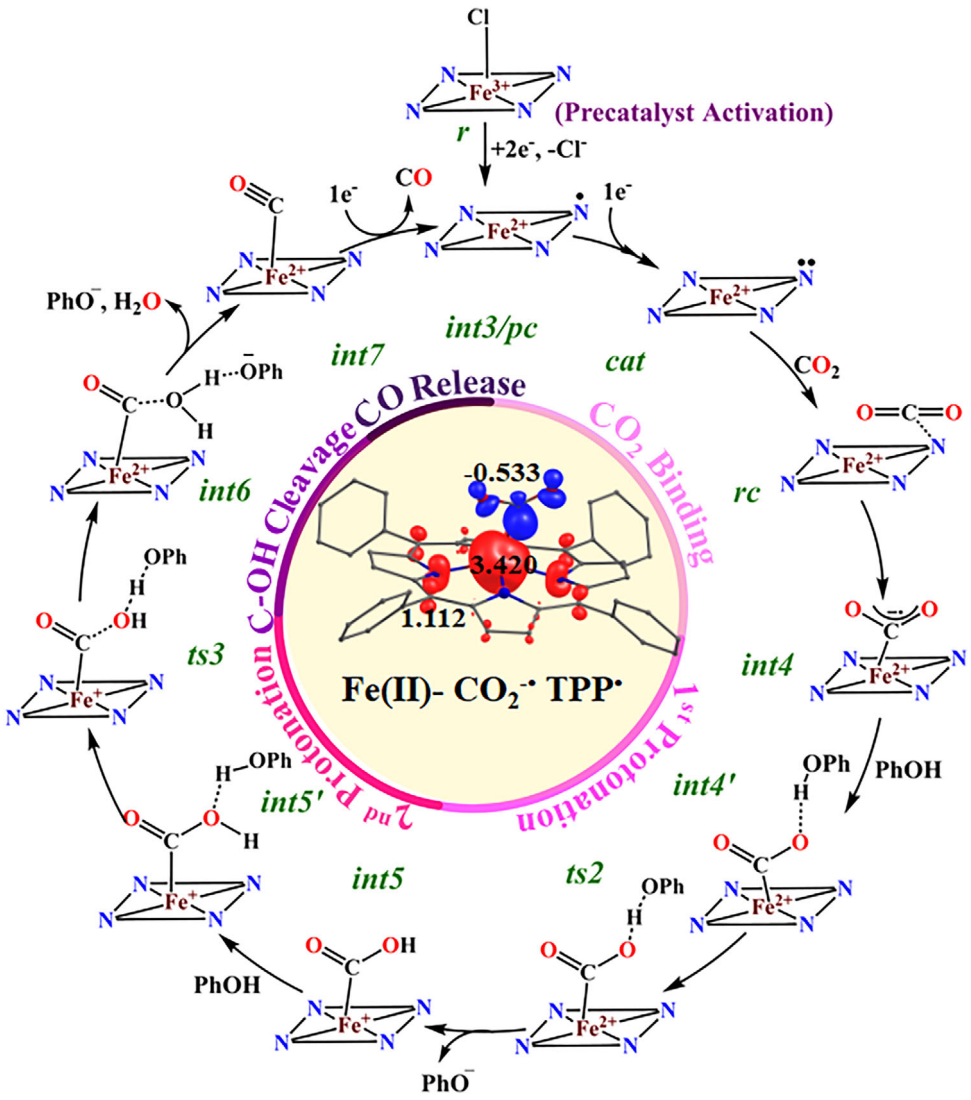

Scheme 2. Schematic representation of the mechanistic pathway for CO_2-to-CO conversion using iron porphyrin systems **1**–**3**.

energetics (exergonic from ***int4*** by 27.5 kJ mol^{-1} for **1** and 8.4 kJ mol^{-1} for **3**), highlighting phenol's dual role as both a proton donor and a key anchoring group that stabilises CO_2 at the Fe centre. Additionally, CO_2 coordination lifts the Fe atom from the basal plane (~0.4–0.5 Å), weakening the Fe–N bonds and stabilising the high-spin state at the Fe centre. A closer look at the electronic structure of this species reveals that the CO_2 molecule, upon binding, is already reduced by one electron, leading to a $CO_2^{-\bullet}$ character, and this is accompanied by a concomitant reduction of β-spin density at the TPP ligand, suggesting electron transfer from the TPP ligand to the CO_2 highlighting the non–innocent role of the ligand in this process (see Scheme 2, Figure S13). Further, the binding has lifted the Fe atom from the basal plane (~0.4–0.5 Å), leading to the weakening of Fe–N bonds and stabilisation of the high-spin state at the Fe centre. This is reflected in the computed orbital energies, particularly the $d_{x^2-y^2}$ orbital is stabilised in ***int4*** (~2.3 eV), resulting in $S_{Fe} = 2$ state, whereas in ***cat***, it lies at ~4.5 eV, resulting in $S_{Fe} = 1$ state. Further, the magnetic coupling at this stage is found to be altered, particularly the interaction between Fe and TPP$^{-\bullet}$ found to be weakly ferromagnetic, while that of $CO_2^{-\bullet}$ is found to be antiferromagnetic ($J_{Fe\text{-}radCO2}$ −2188 cm^{-1}, $J_{Fe\text{-}rad}$ + 57 cm^{-1}). Further, the C─O bond elongation from 1.170 to 1.229 Å (^{5}***1–int4***) and 1.227 Å (^{5}***3–int4***) strongly supports CO_2 radical anion formation (Figure S14).

In the next step, the first protonation is assumed via ***ts2***, leading to the formation of COOH with a barrier of 12.4, 27.9, and 24.9 kJ mol^{-1} for complexes ^{3}***1–ts2***, ^{3}***2–ts2***, and ^{3}***3–ts2***, respectively, and suggestive of a facile proton transfer, though overall energetics are significantly higher and clearly require an electrode potential to drive up the hill. Further, it can be noted that the C─O bond is the least elongated in the case of ^{3}***2–ts2*** (1.278 Å), leading to the highest energy barrier of ~28 kJ mol^{-1} from the preceding species. This is followed by the formation of ***int5***, which is exergonic for complex **3**. Subsequently, a second protonation step occurs via an additional phenol molecule, forming ^{5}***int5'***.[34] The C(O)HO•••H–OPh distances are 1.699, 1.786, and 1.802 Å for complexes **1**, **2**, and **3**, respectively (Figures S15–S21),

with corresponding estimated energies of −7.2, −5.2, and + 53.3 kJ mol^{-1}. Unlike complexes **1** and **2**, where the conversion of ***int5*** to ***int5′*** is exergonic, this step is strongly endergonic for complex **3**. Energy decomposition analysis (EDA) indicates that the origin of this trend lies not in orbital interactions but in the pronounced increase in steric repulsion (+37.7 kJ mol^{-1}) in ***int5′*** relative to ***int5***, which outweighs the modest orbital stabilisation (−21.7 kJ mol^{-1}) (Table S4). Nevertheless, catalyst **3** still has a lower overall energy penalty compared to complexes **1** and **2** (72.7 vis-à-vis 113.3, and 124.4 kJ mol^{-1}).

To assess whether slow proton transfer kinetics in aprotic solvents significantly influence the computed energetics, we evaluated additional mechanistic pathways for ***1–ts2*** and ***1–ts3*** by incorporating explicit DMF and water molecules. The barriers computed for these transition states are marginally higher (by 7–15 kJ mol^{-1}) compared aforementioned barriers, showing that explicit solvent inclusion does not lead to notable changes in the underlying chemistry (Figure S22).

In the next step, H_2O formation occurs via ***ts3***, where the CO(HO)•••H(OPh) bond forms, and the OC•••OH bond cleaves simultaneously, with barriers of 14.8, 15.3, and 18.9 kJ mol^{-1} for ^{5}***1–ts3***, ^{3}***2–ts3***, and ^{3}***3–ts3***, respectively. The resulting Fe(II)–CO complex (^{3}***int6***) is stabilised through (Fe-(O)C•••O(H)H•••$^{-}$OPh) noncovalent interactions with the energy release of 113, 123.4, and 70 kJ mol^{-1} for ***1–3***, respectively. In the next step, the phenoxide and water are assumed to leave, leading to the formation of ***int7*****,** which is also estimated to be exergonic from ***int6***, suggesting facile formation. In the next step, one-electron reduction is hypothesised to trigger the release of CO and regeneration of ***int3***. The reaction is exergonic for **3** (−49.9 kJ mol^{-1}), while **1** and **2** require energy (19.9 and 8.3 kJ mol^{-1}, respectively). However, all species remain energetically favourable compared to ***int3*** (Figure 2). As the modelled reaction corresponds to an electrochemical reduction under a working potential, we have also constructed the potential energy surface at − 1.428 V, the value used in experiments, to demonstrate that the reactions are feasible at this potential, as evidenced by experimental observations (Figure S7).

Additionally, we explored several alternative pathways, including (i) the concerted proton–electron transfer (CPET) mechanism, (ii) Fe–hydride formation, and (iii) bicarbonate generation beyond CO_2 reduction. Among these, both the CPET and ET–PT pathway mentioned earlier remain energetically feasible (194 versus 198 kJ mol^{-1}). In contrast, the Fe–hydride and bicarbonate pathways incur a large energy penalty (>227 kJ mol^{-1}), rendering them unlikely in this setup (see Figure S23).

The catalysts **1**–**3** exhibit different rate-determining steps. For the TPP-ligated catalyst (**1**), CO_2 binding (***ts1'***) is the TOF-determining step, while CO release (***int7***) is the TDI. In catalysts **2** and **3**, the TDTS corresponds to ***ts2*** and ***ts3***, respectively. Using the energetic span model,[35] the overall kinetic barriers are 195.5 (**1**), 184.4 (**2**), and 162.2 kJ mol^{-1} (**3**), indicating that the *o*-TMA-ligated catalyst (**3**) has the highest catalytic efficiency, consistent with experimental results.

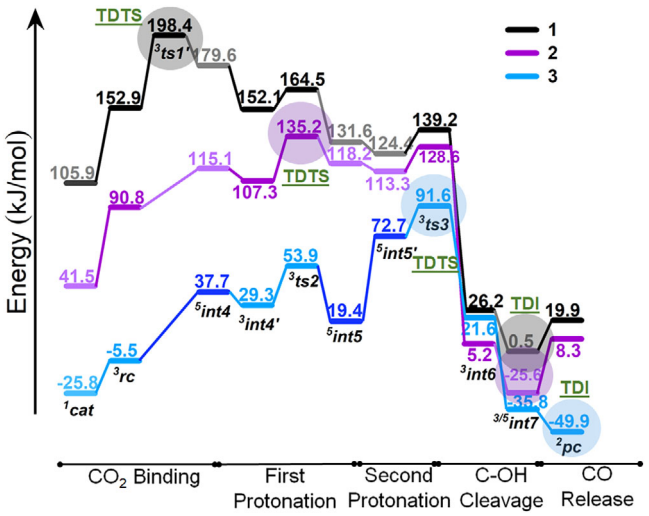

Figure 2. Potential energy diagram for the proposed mechanistic pathway for the formation of active catalyst species (***cat***) for all the complexes **1**–**3**. The colour variation indicates spin transitions through the MECP, where grey, light purple, and dark blue correspond to the S = 2 state, while black, violet, and sky blue represent the S = 1 ground state. Encircled species represent TDTS and TDIs of the reaction.

Correlation to Experiments

(i) To strengthen the correlation between theory and experiment, we computed the spectral features of key intermediates for which experimental data are available. The UV–vis spectrum of ^{6}***1–r*** shows excellent agreement with experiment (cal: λ_{max} = 365, 420, 513, and 575 nm; exp: λ_{max} = 379, 417, 510, and 578 nm; Figure S24). Similarly, the Fe K-edge 1s → 3d transitions are well reproduced, with values for ***1–r*** (cal: 7108.2 eV; exp: 7112.9 eV), ***1–int3*** (cal: 7099.5 eV; exp: 7110.5 eV), and ***1–cat*** (cal: 7099.2 eV; exp: 7110.1 eV; Table S8) closely matching experiment offering, confidence in the estimated electronic structure.[32] In addition, the computed IR frequencies for key intermediates, weakly bound CO_2 (2417 cm^{-1}, exp. ~2349 cm^{-1}), $CO_2^{\bullet-}$ radical anion[36] (1892 cm^{-1}, exp. ~1665 cm^{-1}), metal-bound COOH[37] (1760 cm^{-1}, exp. ~1750 cm^{-1}), and Fe–CO[38,39](2167 cm^{-1}, exp. ~2143 cm^{-1}) match experimental values closely, further supporting the reliability of our computational predictions. (ii) Experimental studies report the highest reactivity for **3** with E^{0}_{cat} = −0.944 V versus SHE[40]), followed by **2** (−1.263 V) and **1** (−1.428 V), trends that are well reproduced in our calculations[41] (E^{0}_{cat} = −1.104 V for **3**, −1.264 V for **2**, and −1.477 V for **1** versus SHE, and see Supporting Information for a detailed discussion on the procedure employed for this calculations and Figure S25). (iii) Our calculations confirm a triplet ground state for ***int2***, which is in agreement with experimental studies. This is further supported by the measured magnetic moment range (4.0–4.4 μB), consistent with S = 1 and a significant zero-field splitting (D).[33,42,43] (iv) Our computed electronic structures align well with experimental data, confirming ligand-centred reductions.[32,44] The Fe centre retains an intermediate-spin Fe(II) state, with strong antiferromagnetic coupling observed

between the Fe centre and ligand-based radicals, validating the predicted non-innocent behaviour of the porphyrin ligand and earlier reports. (v) we identify CO_2 binding to Fe and forming $CO_2^{\bullet-}$ as the rate-determining step (TOF determining transition state as per energetic span model[35]) for **1**, aligning with experimental CV and KIE studies.[45,46] For **2** and **3**, CO_2 binding is not steeply energy demanding, and this shifts the TDTS to the first and second protonation steps, respectively. This trend is supported by K_{CO2} values, which indicate that the electronic effects of meso substituents influence Fe's electron density, facilitating CO_2 activation and altering the corresponding rate-limiting steps.[47] (vi) The experimental TOF for the CO_2-to-CO conversion with catalyst **3** is reported to be 10^6 s^{-1} at an overpotential of 220 mV. We calculated the TOF based on Equation S1 using the energetic span model, resulting in 0.2×10^5 s^{-1}. This value closely aligns with the experimental value, solidifying the reliability of our approach.

Effect of Local and Oriented External Electric Field

To investigate whether the enhanced catalytic efficiency observed for **2** and **3** is linked to the generation of a LEF by the charged substituents, we quantified the LEF exerted by the TMA groups along the Fe–N_{TMA} directions for **2** and **3**, and along the Fe–$C_{p\text{–phenyl}}$ axis for **1**, as illustrated in Figure S26, using the TITAN code. The positively charged TMA substituents introduce a significant electrostatic influence, while the TPP nitrogen atoms carry a substantial negative charge. This charge distribution effectively establishes an internal dipole, aligning a directional electric field within the system. Such an oriented LEF can play a pivotal role in stabilising key intermediates and transition states involved in CO_2 reduction, particularly the formation of the CO_2 radical anion (CO_2^-). Similar to the role of LEF in enzymatic and synthetic catalytic systems, the LEF generated in **2** and **3** under electrochemical conditions is expected to align with the applied field and reduce the overpotential by facilitating the electron transfer to CO_2, enhancing its activation and subsequent conversion to CO.

The LEFs at the Fe centre for ***1–cat*** are -7.70×10^{-4}, -7.89×10^{-4}, 7.64×10^{-4}, and 7.83×10^{-4} V $Å^{-1}$ along the four Fe–C axes, resulting in a net field of 6.68×10^{-5} V $Å^{-1}$ (see Supporting Information for the details). In contrast, ***2–cat*** and ***3–cat*** exhibit significantly stronger LEFs of 1.28×10^{-3} and 8.00×10^{-3} V $Å^{-1}$, respectively, due to the positively charged TMA substituents. This trend aligns with experimental findings [20] where increased LEFs enhance TOF beyond 10^6 s^{-1} at low overpotentials. Since the rate of the reaction depends on the TDTS and TDI of the reaction, we extended our study to find the LEF on these species of these three complexes and found the same order in all cases, representing that the trend in reactivity is directly correlated with the LEF at critical stages of the reaction (see Figures 3a and S27).

Since TDTS and TDI govern the rate of CO_2 reduction, we investigated the LEF at these critical points to establish a direct correlation between electrostatic effects and catalytic efficiency. Our analysis reveals that for the

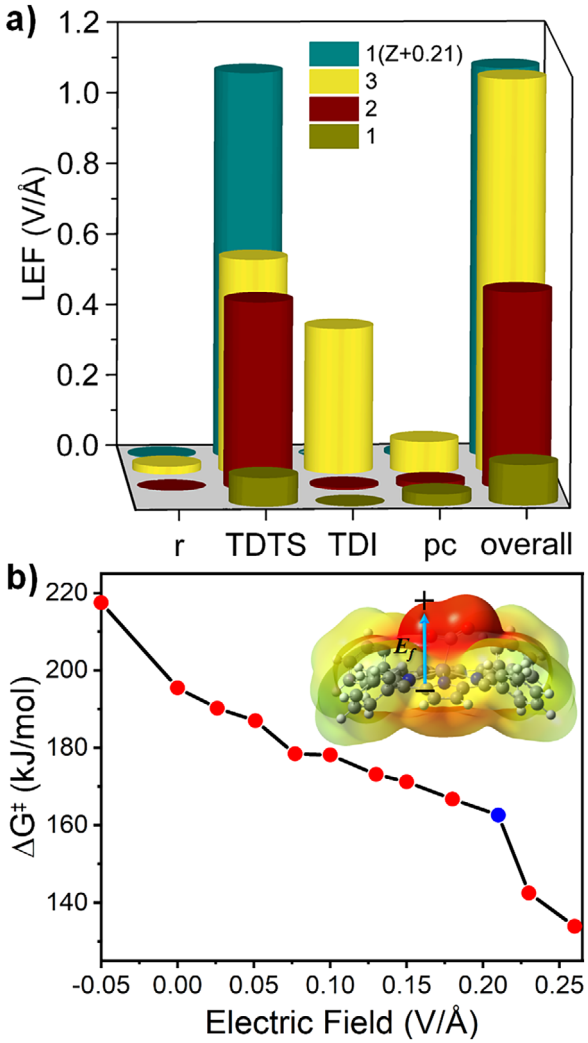

Figure 3. a) Computed local electric field (LEF, in V $Å^{-1}$) at key catalytic intermediates (r, TDTS, TDI, pc). b) Effect of OEEFs on the energy barrier of complex **1**.

TDTS, the LEF follows the order **3** (0.6033 V $Å^{-1}$) > **2** (0.5267 V $Å^{-1}$) > **1** (0.0799 V $Å^{-1}$), indicating that the stronger electrostatic stabilisation in **2** and **3** significantly reduces the activation barrier. Similarly, for the TDI, the LEF values are 0.4080 (**3**), 0.0060 (**2**), and 0.0010 V $Å^{-1}$ (**1**), confirming the enhanced stabilisation of key intermediates in **3**. This trend directly correlates with the observed catalytic efficiency.

To probe the role of external electric field modulation on the reactivity, we have studied species ***1–int3***, ***1–ts1'***, ***1–int7***, and ***1–pc*** under varying OEEFs from −0.10 to 0.26 V $Å^{-1}$ along the Fe–C_{CO2} axis. The overall energy barriers were computed using the energy span model, defined as:

$$\Delta G^{\ddagger} = (\Delta G_{TDTS} - \Delta G_{TDI} + \Delta G_r) \quad (1)$$

Under an OEEF of 0.21 V $Å^{-1}$, the overall energy barrier for **1** drops to 162.6 kJ mol^{-1} (Figure 3b, blue circle), demonstrating that an external field can effectively

enhance catalytic performance by stabilising (destabilising) the TDTS (TDI) and lowering the kinetic barrier. Further, the TITAN code also estimates that the LEF computed at the OEEF geometries (1.1003 V Å^{-1} at Z + 0.21 V Å^{-1} for **1** versus 1.1085 V Å^{-1} for **3**) closely matches the one computed above, reiterating the role of the electrostatic environment playing a dominant role in controlling the reactivity. These findings establish a direct relationship between LEF, OEEF, and catalytic activity, offering a mechanistic framework for designing efficient electrochemical CO_2 reduction catalysts.

Prediction of Novel Fe–TPP Models for CO_2 Reduction

In the next step, we modelled a series of modified Fe–porphyrin complexes in which different charged or electron-donating groups were strategically introduced based on earlier learnings. These included systems bearing one, two, or three TMA substituents at the ortho positions of the phenyl rings (Fe-1-TMA, Fe-2-TMA, and Fe-3-TMA), a porphyrin carrying a $CH_2NH_3^+$ group at a meso position (Fe-$CH_2NH_3^+$), a variant with four PMe_3 donors at ortho positions (Fe–o-PMe_3), a complex substituted with sulfonyl anisole groups at para positions (Fe–p-S(PhOMe)$_2$), and a porphyrin containing TMA groups at both ortho and para sites (Fe–o,*p*-TMA) (see Figure S28). In the next step, the rate-limiting step, i.e., ***ts3*,** has been computed for these models (see Figure S29). The computed calculations reveal a systematic relationship between the LEF and the activation barriers ($\Delta G^{\ddagger}$) for the series of Fe–porphyrin complexes. Among the asymmetrically substituted TMA derivatives, Fe-3-TMA, Fe-2-TMA, and Fe-1-TMA display progressively higher activation barriers of 175.6, 179.9, and 188.6 kJ mol^{-1}, respectively, which correlate with their LEF$_r$ values of 0.0154, 0.0144, and 2.1 × 10^{-4} V Å^{-1}. This trend underscores that stronger and more optimally oriented LEFs significantly stabilise the transition state, lowering the $\Delta G^{\ddagger}$. Similarly, other variants further illustrate this principle: Fe–o-PMe_3, with an LEF$_r$ of 0.0182 V Å^{-1}, achieves a moderately low barrier of 174.2 kJ mol^{-1}, whereas Fe–p-S(PhOMe)$_2$ and Fe-$CH_2NH_3^+$, featuring less favourable field orientations, display higher barriers of 184.2 kJ mol^{-1} and correspondingly smaller LEF contributions. The Fe–*o,p*-TMA system exhibits the lowest barrier in the series ($\Delta G^{\ddagger}$ = 129.4 kJ mol^{-1}) and the largest LEF$_r$ of 0.0313 V Å^{-1}, clearly highlighting the beneficial effect of maximising field magnitude and aligning its vector with the reactive axis.

Discussion

The electrochemical conversion of CO_2 into value-added chemicals remains one of the foremost challenges in sustainable chemistry, with the reduction to CO serving as a key step. Among the most efficient catalysts for this transformation are iron porphyrin (Fe-TPP) derivatives. Despite extensive studies on substituted Fe-TPP systems, their catalytic activity varies significantly, from complete inactivity with sulfonyl groups to remarkably high turnover frequencies (TOFs) of up to 10^6 s^{-1} with trimethylamine substituents. While electronic and steric effects have been widely considered, the exceptional performance of positively charged species has remained poorly understood. In this work, we investigate a series of Fe-TPP complexes and reveal that local electric fields (LEFs), often overlooked, act as a critical and unifying factor governing reactivity. This insight offers a predictive framework for rational catalyst design.

Our initial electronic structure analysis of key intermediates involved in the catalytic cycle reveals that the redox non-innocent nature of the TPP ligand plays a central role in modulating reactivity. The ability of TPP to host radical character, as evident in the formation of species like [Fe(II)TPP$^{\bullet-}$]$^-$ and [Fe(II)TPP$^{\bullet\bullet}$]$^{2-}$, is supported by strong antiferromagnetic coupling between the Fe centre and the ligand (J = −889 cm^{-1} for ***1-int3***), indicative of substantial metal–ligand electronic communication. This non-innocence facilitates access to low-valent states via ligand-based reductions and enables reversible electron delocalisation between the metal and the π-system during catalysis, effectively tuning redox potentials and stabilising key intermediates. Furthermore, the substituents on the TPP ring, especially electron-donating groups like TMA, impact the reactivity not only via inductive effects but also by modulating the extent of ligand participation in redox processes. This behaviour aligns well with prior experimental findings and spectroscopic signatures, including Mössbauer and X-ray absorption studies,[32,33] further corroborating the central role of porphyrin non-innocence in dictating electrocatalytic efficiency.

Secondly, we explored the mechanism of CO_2 to CO conversion for catalysts **1**–**3**, and the relative energetics of key intermediates, benchmarked against the most efficient catalyst **3** (Figure 4a), confirms the reactivity order **3** > **2** > **1**, in agreement with the experimental report.[20] Notably, the catalysts exhibit different rate-determining steps: for **1**, CO_2 binding is the TOF-determining step and CO release the TDI; in contrast, **2** and **3** proceed via distinct transition states (first protonation of CO_2 and CO release), with energy span analysis yielding kinetic barriers of 195.5, 184.4, and 162.2 kJ mol^{-1} for **1**–**3**, respectively, establishing **3** as the most efficient catalyst.

To probe the origin of the difference in reactivity in catalysts **1**–**3**, we sought to understand the underlying origin of their reactivity differences. Our analysis revealed that the LEF, induced by charged substituents such as the TMA groups, plays a decisive role, surpassing conventional steric or electronic factors, in modulating both the reduction potential and the energy landscape of the rate-determining steps. To isolate the influence of LEF from other substituent effects, we applied an oriented external electric field (OEEF) to the unsubstituted complex **1**, calibrated to match the LEF magnitude computed for catalyst **3**. Remarkably, this field-altered system reproduced the energy barrier of **3** (~162.2 versus 162.6 kJ mol^{-1}) at **1** (Z + 0.21 V Å^{-1}), confirming that the LEF alone can account for the observed catalytic enhancement. Such field effects are fully consistent

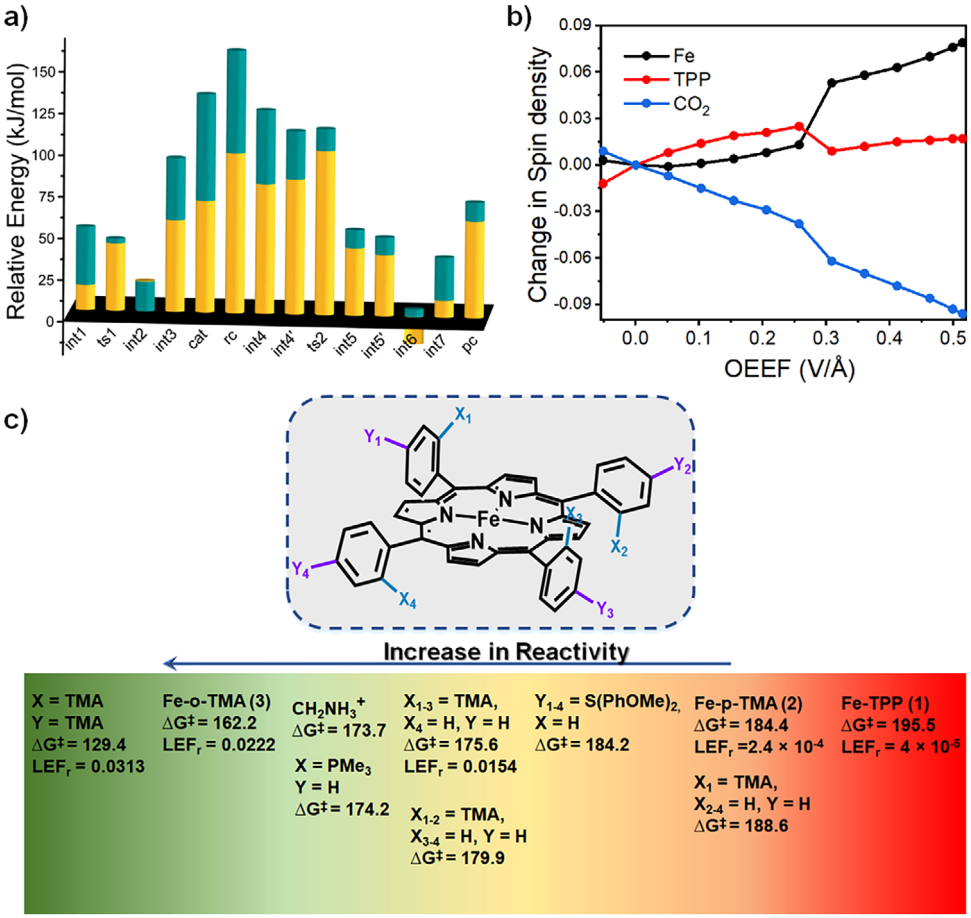

Figure 4. a) DFT computed relative energies of **1** (teal) and **2** (yellow) with respect to **3** for catalytic conversion, b) change in spin densities of Fe, TPP and CO_2 by ss in ***1-int4***, and c) different Fe-porphyrin-based catalysts model structures arranged in the reactivity order where $\Delta G^{\ddagger}$ represents overall energy barrier (kJ mol^{-1}) and LEF_r is the quantified LEF for ***r*** (in V $Å^{-1}$).

with electrochemical environments: in real Helmholtz layers at charged electrodes, local electric fields on the order of 0.1–1.0 V $Å^{-1}$ are considered realistic.[48] Quantification of LEFs at the TDTS and TDI stages further corroborates this trend, with stronger internal fields in **2** ($LEF_r = 2.4 \times 10^{-4}$ V $Å^{-1}$, $LEF_{TDTS} = 0.52$ V $Å^{-1}$) and **3** ($LEF_r = 2.2 \times 10^{-2}$ V $Å^{-1}$, $LEF_{TDTS} = 0.66$ V $Å^{-1}$) correlating with reduced activation barriers and improved reactivity as compared to **1** ($LEF_r = 4 \times 10^{-5}$ V $Å^{-1}$, $LEF_{TDTS} = 0.80$ V $Å^{-1}$). These findings highlight the central role of electrostatic fields—whether internally generated or externally applied—in governing catalytic efficiency in electrochemical CO_2 reduction. Beyond energetics, electric field induced spin density analyses revealed a striking redistribution of unpaired electron density: spin density shifts from the iron centre to the porphyrin ligand, while CO_2 gains negative spin density (Figure 4b). This again underscores that the porphyrin macrocycle is not a passive spectator but actively engages in redox processes during catalysis.

Guided by the hypothesis that local electric fields (LEFs), govern catalytic efficiency, we systematically designed a library of Fe-porphyrin catalysts with varied substitution patterns, as summarised in Figure 4c. These models span a wide reactivity spectrum, with energy barriers ($\Delta G^{\ddagger}$) ranging from 129.4 to 195.5 kJ mol^{-1} and varying LEF values. Among them, the Fe-di-ortho, para-TMA system, featuring two TMA groups on both ortho and para positions, exhibits the lowest energy barrier ($\Delta G^{\ddagger}$ = 129.4 kJ mol^{-1}) and the highest LEF_r (0.0313 V $Å^{-1}$), highlighting the beneficial effect of strategic charge orientation. Following this, Fe–o-TMA, with an LEF of 0.0222 V $Å^{-1}$, achieves a barrier of 162.2 kJ mol^{-1}, again emphasising the catalytic advantage of favourable LEF alignment.

We also examined asymmetrically substituted systems by selectively introducing *o*-TMA groups on varying numbers of phenyl rings and extended this approach to alternative donors such as $-PMe_3$ and $-S(PhOMe)_2$, revealing a clear trend of increasing activation barriers that underscores the impact of substituent identity and placement on catalytic performance. These models clearly demonstrate that the nature and position of local charges, such as ortho versus para substitution and the identity of donor atoms like phosphorus and sulphur, show a strong correlation with the computed barrier heights and offer a promising strategy to fine-tune catalytic performance. Importantly, not just the presence but the precise positioning and orientation of charged groups shape the local electrostatic environment, thereby directly influencing catalytic efficiency.

Conclusion

Using a combination of density functional theory and response theory (which incorporates electric field effects), we investigated the longstanding challenge of improving CO_2 to CO catalytic conversion. Our study centres on Fe tetraphenyl porphyrin analogues, widely regarded as benchmark catalysts for this transformation. We reveal that the TPP ligand is not merely a passive scaffold but exhibits radical character that promotes exchange coupling with the metal centre, playing a direct role in the catalytic mechanism. While substituents on the phenyl rings were previously assumed to influence reactivity only through steric or electronic factors, we find their dominant effect arises from inducing local electric fields that modulate reduction potentials and lower activation barriers at key steps. Remarkably, applying an oriented external electric field mimics the reactivity of top-performing catalysts, and guided by this understanding, we propose new molecular designs that surpass current systems, paving the way for a next-generation design strategy in this well-established field.

Acknowledgements

P.D. thanks PMRF for the fellowship. G.R. would like to thank DST and SERB (SB/SJF/2019-20/12; CRG/2022/001697) for funding.

Conflict of Interests

The authors declare no conflict of interest.

Data Availability Statement

The data that support the findings of this study are available in the Supporting Information of this article.

Keywords: CO_2 reduction · Density functional theory · Electrocatalysis · Mechanistic studies · Metalloporphyrins

[1] Y. Y. Birdja, E. Pérez-Gallent, M. C. Figueiredo, A. J. Göttle, F. Calle-Vallejo, M. T. Koper, *Nat. Energy* **2019**, *4*, 732–745. https://doi.org/10.1038/s41560-019-0450-y.
[2] D. Gao, R. M. Arán-Ais, H. S. Jeon, B. R. Cuenya, *Nat. Catal.* **2019**, *2*, 198–210. https://doi.org/10.1038/s41929-019-0235-5.
[3] X. Su, X.-F. Yang, Y. Huang, B. Liu, T. Zhang, *Acc. Chem. Res.* **2019**, *52*, 656–664. https://doi.org/10.1021/acs.accounts.8b00478.
[4] Q. Zhu, *Clean Energy* **2019**, *3*, 85–100. https://doi.org/10.1093/ce/zkz008.
[5] P. M. Forster, C. Smith, T. Walsh, W. F. Lamb, R. Lamboll, B. Hall, M. Hauser, A. Ribes, D. Rosen, N. P. Gillett, *Earth Syst. Sci. Data* **2024**, *16*, 2625–2658. https://doi.org/10.5194/essd-16-2625-2024.
[6] G. Velmurugan, P. Baur, P. Comba, *Angew. Chem.* **2024**, *136*, e202319530. https://doi.org/10.1002/ange.202319530.
[7] Z. Yin, M. Zhang, Y. Long, H. Lei, X. Li, X. P. Zhang, W. Zhang, U. P. Apfel, R. Cao, *Angew. Chem. Int. Ed.* **2025**, *64*, e202500154. https://doi.org/10.1002/anie.202500154.
[8] J. Hädeler, G. Velmurugan, R. Lauer, R. Radhamani, F. Keppler, P. Comba, *J. Am. Chem. Soc.* **2023**, *145*, 24590–24602.
[9] P. Dua, A. Sen, G. Rajaraman, *Chem. - Eur. J.* **2024**, *30*, e202401796. https://doi.org/10.1002/chem.202401796.
[10] D. U. Nielsen, X.-M. Hu, K. Daasbjerg, T. Skrydstrup, *Nat. Catal.* **2018**, *1*, 244–254. https://doi.org/10.1038/s41929-018-0051-3.
[11] A. Sen, M. Ansari, G. Rajaraman, *Inorg. Chem.* **2023**, *62*, 3727–3737. https://doi.org/10.1021/acs.inorgchem.2c02812.
[12] A. Singh, A. Zamader, R. Khakpour, K. Laasonen, M. Busch, M. Robert, *J. Am. Chem. Soc.* **2024**, *146*, 22129–22133. https://doi.org/10.1021/jacs.4c06878.
[13] C. Xu, P. Hong, Y. Dong, M. Robert, G. Shao, Y. Lei, *Adv. Energy Mater.* **2025**, 2406146, https://doi.org/10.1002/aenm.202406146.
[14] T. Lin, Y. An, F. Yu, K. Gong, H. Yu, C. Wang, Y. Sun, L. Zhong, *ACS Catal.* **2022**, *12*, 12092–12112. https://doi.org/10.1021/acscatal.2c03404.
[15] M. Xu, Z.-w. Qu, S. Grimme, D. W. Stephan, *J. Am. Chem. Soc.* **2021**, *143*, 634–638. https://doi.org/10.1021/jacs.0c11482.
[16] C. Costentin, M. Robert, J.-M. Savéant, A. Tatin, *Proc. Natl. Acad. Sci. U.S.A.* **2015**, *112*, 6882–6886. https://doi.org/10.1073/pnas.1507063112.
[17] B. Mondal, P. Sen, A. Rana, D. Saha, P. Das, A. Dey, *ACS Catal.* **2019**, *9*, 3895–3899. https://doi.org/10.1021/acscatal.9b00529.
[18] J. Bonin, M. Chaussemier, M. Robert, M. Routier, *ChemCatChem* **2014**, *6*, 3200–3207. https://doi.org/10.1002/cctc.201402515.
[19] R. B. Ambre, Q. Daniel, T. Fan, H. Chen, B. Zhang, L. Wang, M. S. Ahlquist, L. Duan, L. Sun, *Chem. Commun.* **2016**, *52*, 14478–14481. https://doi.org/10.1039/C6CC08099E.
[20] I. Azcarate, C. Costentin, M. Robert, J.-M. Savéant, *J. Am. Chem. Soc.* **2016**, *138*, 16639–16644. https://doi.org/10.1021/jacs.6b07014.
[21] S. Shaik, D. Danovich, J. Joy, Z. Wang, T. Stuyver, *J. Am. Chem. Soc.* **2020**, *142*, 12551–12562. https://doi.org/10.1021/jacs.0c05128.
[22] S. A. Siddiqui, K. D. Dubey, *Phys. Chem. Chem. Phys.* **2022**, *24*, 1974–1981. https://doi.org/10.1039/D1CP03978D.
[23] S. Yadav, S. Shaik, S. A. Siddiqui, S. Kalita, K. D. Dubey, *J. Chem. Inf. Model.* **2022**, *62*, 1025–1035. https://doi.org/10.1021/acs.jcim.1c01453.
[24] D. Bím, A. N. Alexandrova, *ACS Catal.* **2021**, *11*, 6534–6546.
[25] S. Yu, P. Vermeeren, T. A. Hamlin, F. M. Bickelhaupt, *Chem. - Eur. J.* **2021**, *27*, 5683–5693 https://doi.org/10.1002/chem.202004906.
[26] M. T. Blyth, M. L. Coote, *Phys. Chem. Chem. Phys.* **2023**, *25*, 375–383. https://doi.org/10.1039/D2CP04507A.
[27] S. A. Siddiqui, T. Stuyver, S. Shaik, K. D. Dubey, *Jacs Au* **2023**, *3*, 3259–3269. https://doi.org/10.1021/jacsau.3c00536.
[28] P. Sreelakshmi, R. Mahashaya, S. Leitherer, U. Rashid, J. M. Hamill, M. Nair, P. Rajamalli, V. Kaliginedi, *J. Am. Chem. Soc.* **2024**, *146*, 35242–35251. https://doi.org/10.1021/jacs.4c12423.
[29] F. Paulat, N. Lehnert, *Inorg. Chem.* **2008**, *47*, 4963–4976. https://doi.org/10.1021/ic8002838.
[30] N. A. Stephenson, A. T. Bell, *Inorg. Chem.* **2006**, *45*, 5591–5599. https://doi.org/10.1021/ic0521067.
[31] J.-M. Savéant, *Chem. Rev.* **2008**, *108*, 2348–2378. https://doi.org/10.1021/cr068079z.
[32] C. Römelt, J. Song, M. Tarrago, J. A. Rees, M. van Gastel, T. Weyhermüller, S. DeBeer, E. Bill, F. Neese, S. Ye, *Inorg. Chem.* **2017**, *56*, 4745–4750. https://doi.org/10.1021/acs.inorgchem.7b00401.

[33] M. Tarrago, C. Römelt, J. Nehrkorn, A. Schnegg, F. Neese, E. Bill, S. Ye, *Inorg. Chem.* **2021**, *60*, 4966–4985. https://doi.org/10.1021/acs.inorgchem.1c00031.
[34] C. Costentin, M. Robert, J.-M. Savéant, *Acc. Chem. Res.* **2015**, *48*, 2996–3006. https://doi.org/10.1021/acs.accounts.5b00262.
[35] S. Kozuch, S. Shaik, *Acc. Chem. Res.* **2011**, *44*, 101–110. https://doi.org/10.1021/ar1000956.
[36] K. Hartman, I. Hisatsune, *J. Chem. Phys.* **1966**, *44*, 1913–1918. https://doi.org/10.1063/1.1726961.
[37] K. Saito, T. Xu, H. Ishikita, *J. Phys. Chem. B* **2022**, *126*, 4999–5006. https://doi.org/10.1021/acs.jpcb.2c02193.
[38] G. E. Ewing, G. C. Pimentel, *J. Chem. Phys.* **1961**, *35*, 925–930. https://doi.org/10.1063/1.1701239.
[39] C. Lamberti, S. Bordiga, F. Geobaldo, A. Zecchina, C. Otero Areán, *J. Chem. Phys.* **1995**, *103*, 3158–3165. https://doi.org/10.1063/1.470249.
[40] A. A. Isse, A. Gennaro, *J. Phys. Chem. B* **2010**, *114*, 7894–7899. https://doi.org/10.1021/jp100402x.
[41] L. Castro, M. Bühl, *J. Chem. Theory Comput.* **2014**, *10*, 243–251. https://doi.org/10.1021/ct400975w.
[42] H. Goff, G. N. La Mar, C. A. Reed, *J. Am. Chem. Soc.* **1977**, *99*, 3641–3646. https://doi.org/10.1021/ja00453a022.
[43] G. Lang, K. Spartalian, C. A. Reed, J. P. Collman, *J. Chem. Phys.* **1978**, *69*, 5424–5427. https://doi.org/10.1063/1.436532.
[44] T. Mashiko, C. A. Reed, K. J. Haller, W. R. Scheidt, *Inorg. Chem.* **1984**, *23*, 3192–3196. https://doi.org/10.1021/ic00188a032.
[45] M. Hammouche, D. Lexa, M. Momenteau, J. M. Saveant, *J. Am. Chem. Soc.* **1991**, *113*, 8455–8466. https://doi.org/10.1021/ja00022a038.
[46] W. Deng, P. Zhang, B. Seger, J. Gong, *Nat. Commun.* **2022**, *13*, 803. https://doi.org/10.1038/s41467-022-28436-z.
[47] H. He, Z.-Y. Qiu, Z. Yin, J. Kong, J.-S. Dang, H. Lei, W. Zhang, R. Cao, *Chem. Commun.* **2024**, *60*, 5916–5919. https://doi.org/10.1039/D4CC01630K.
[48] L. D. Chen, M. Urushihara, K. Chan, J. K. Nørskov, *ACS Catal.* **2016**, *6*, 7133–7139. https://doi.org/10.1021/acscatal.6b02299.

Manuscript received: September 24, 2025
Revised manuscript received: October 21, 2025
Manuscript accepted: October 21, 2025
Version of record online: November 05, 2025